Poststack and prestack depth migrations using Hale's extrapolator

Saleh M. Al-Saleh, John C. Bancroft, and Hugh D. Geiger

ABSTRACT

Recursive wavefield extrapolation methods in the space-frequency domain are popular because they are powerful in handling strong lateral velocity variations. However, one of the problems of these methods is the instability of the extrapolation operator. Unstable operators tend to amplify the extrapolated wavefield at each depth step.

The Hale's method can design stable extrapolation operators. One of the advantages of Hale's extrapolator is that it is fairly stable where it does not amplify the extrapolated wavefield at each depth step. The impulse response of Hale's extrapolator and the poststack migration of Marmousi dataset show that it can handle lateral velocity variations but not the steeply dipping events. Hale's extrapolator may be a good candidate for data that have moderate dips, but probably not for steeply dipping events.

Some applications of Hale's extrapolator in prestack depth migration with different imaging conditions are shown. The different imaging conditions give different amplitudes of the same reflector. Only the deconvolution imaging condition can preserve the amplitude of the reflector.

INTRODUCTION

To derive the Hale's extrapolator, we start with the 2-D scalar wave equation

$$\frac{\partial^2 \psi}{\partial x^2} + \frac{\partial^2 \psi}{\partial z^2} = \frac{1}{V^2}\frac{\partial^2 \psi}{\partial t^2}. \tag{1}$$

After taking 2-D Fourier transform, Equation 1 becomes

$$\frac{\partial^2 \bar{\tilde{\psi}}}{\partial z^2} = -k_z{}^2 \bar{\tilde{\psi}} \tag{2}$$

where

$$k_z{}^2 = \frac{\omega^2}{V^2} - k_x{}^2. \tag{3}$$

Equation 2 is just a 1D Helmholtz equation whose solution, for upgoing or downgoing waves, is

$$\bar{\tilde{\psi}}\left(k_x, z, \omega\right) = \bar{\tilde{\psi}}\left(k_x, z = 0, \omega\right) e^{ik_z z}. \tag{4}$$

Note that ψ is the wavefield representing pressure, $\bar{\tilde{\psi}}$ represents its 2-D Fourier transform, t is the two-way travel time, and *x* and *z* are the horizontal and vertical coordinates. So the wavefield at some depth *z*, $\bar{\tilde{\psi}}\left(k_x, z, \omega\right)$ can be obtained by

multiplying the recoded wavefield at the surface, $\bar{\bar{\psi}}(k_x, z=0, \omega)$, by a phase shift operator, $e^{ik_z z}$ if the velocity is constant. This is the phase shift migration that was first introduced by Gazdag (1978).

It is not immediately apparent how lateral velocity variations can be handled using the Gazdag phase shift method because the space coordinate has been Fourier transformed. As a result, extrapolation techniques for a laterally variable velocity field are usually formulated in the space-frequency domain (Gazdag 1980, Berkhout 1984, Holberg 1988, Hale 1991, and others) as a dip-limited approximation to the inverse Fourier transform of the phase shift operator. To handle lateral velocity variations, the extrapolator is varied with the local velocity of the computation grid. For example, the wavefield at depth= $z + \Delta z$ can at some x-location, can be computed by:

(a) designing an operator in the frequency-wavenumber domain using the velocity of that output point,

(b) applying an inverse Fourier transform to the extrapolator from the frequency-wavenumber to the frequency-space domains ,

then applying this extrapolator in the $\omega - x$ domain as a convolution process between the extrapolator and the wavefield at depth=z.

The extrapolator has to have a finite length, which means the inverse Fourier transform of the extrapolator from the frequency-wavenumber to the space-frequency must be truncated. Truncation with a boxcar in the space-frequency domain is equivalent to convolving the Fourier transform of the extrapolator with a *sinc* function, which is the Fourier transform of the boxcar. Since the amplitude and phase spectra of the extrapolator in the frequency-wavenumber domain have discontinuities at the evanescent boundary, convolving with a *sinc* function results in an overshoot at this boundary, "Gibbs Phenomena" (Figure 1). This truncated extrapolator is not stable, as the amplitude exceeds unity, and repeated applications of it will cause amplitudes greater than one to accumulate.

There are different methods for designing explicit stable extrapolators such as the constrained least-squares method (Holberg, 1988), the modified Taylor series method (Hale, 1991), and the weighted least squares optimization (Thorbecke, 2004).

In this report, Hale's method for designing explicit stable extrapolation operators will be reviewed. One way to stabilize the extrapolator is also shown. The impulse response and the poststack depth migration of the Marmousi dataset will be used to evaluate the extrapolator. Some applications of the extrapolator in prestack depth migration with different imaging conditions are also shown. Using Hale's extrapolator, the different imaging conditions are investigated to see how they handle the amplitudes of the reflectors.

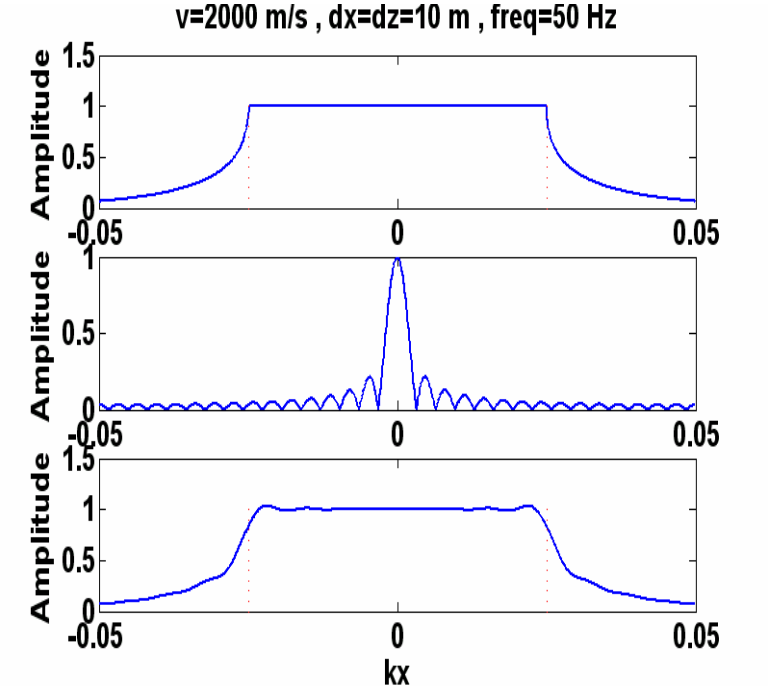

FIG 1. Convolving the frequency-wavenumber spectrum of the (the top row) with a sinc function (the middle row) results in an overshoot at the evanescent boundary (bottom row). The dashed line shows the evanescent boundary.

THEORY OF HALE'S EXTRAPOLATOR

A brief review of Hale's method is presented here. Let's denote the desired phase shift operator by

$$D(k) = e^{ik_z \Delta z}, \tag{5}$$

where

$$k_z = \left(\frac{1}{\Delta x}\right)\left[\left(\frac{\omega \Delta x}{v}\right)^2 - k^2\right]^{1/2}, \tag{6}$$

and

$$k = \Delta x k_x. \tag{7}$$

We can rewrite Equation 5 as

$$D(k) = \exp\left(i\left(\frac{\Delta z}{\Delta x}\right)\left[\left(\frac{\omega \Delta x}{v}\right)^2 - k^2\right]^{1/2}\right) \tag{8}$$

Note that the quantities $\omega\Delta x/v$ and k have been normalized. The normalization of $\Delta z/\Delta x$ and $\omega\Delta x/v$ uniquely determine the desired transform, $D(k)$. The transform $D(k)$ is the same term as that applied in the phase-shift migration and can only handle velocity varying with depth. For a general inhomogeneous medium with significant lateral velocity variations, downward continuation can be carried out conveniently in the $\omega - x$ domain as a dependant convolution (Holberg, 1988).

The symmetry of the desired transform, $D(k)$, with respect to k implies that the complex extrapolation filter coefficients, h_n (the actual extrapolator in the $\omega - x$ domain), should be even. Specifically, we expect: $h_{-n} = h_n$. Therefore, the number of coefficients N should be odd, with the coefficient index n bounded by $-(N-1)/2 \le n \le (N-1)/2$. Due to the symmetry of h_n, the filter can be specified by (N+1)/2 complex coefficients, where N denotes the number of complex coefficients needed to define the extrapolation filter. The Fourier transform of the extrapolation filter is defined by

$$H(k) = \sum_{n=-(N-1)/2}^{(N-1)/2} h_n e^{-ikn}. \tag{9}$$

Because of the symmetry of h_n,

$$H(k) = \sum_{n=0}^{(N-1)/2} (2-\delta_{n0})\, h_n \cos(kn), \tag{10}$$

where δ_{n0} is the Kronecker delta function defined by

$$\delta_{n0} = \begin{cases} 1, & if \;\; n = 0 \\ 0, & otherwise \end{cases}. \tag{11}$$

In Hale's method, the coefficients of the filter are represented as a sum of M weighted basis functions:

$$h_n = \sum_{m=0}^{M-1} c_m b_{mn}, \tag{12}$$

where a good choice for the basis functions is

$$b_{mn} = \left(2 - \delta_{m0}\right) \cos\left(\frac{2\pi mn}{N}\right). \tag{13}$$

In Hale's method, instead of determining $(N+1)/2$ complex filter coefficients, only M complex weights c_m are determined. To ensure stability, the number, M, of weights must be less than the number $(N+1)/2$ complex filter coefficients. Therefore, only the first M even derivatives of the desired and the actual Fourier transforms are matched and the remaining $(N+1)/2 - M$ degrees of freedom are used to ensure stability. To determine c_m, we begin with the Fourier transform of the extrapolation filter

$$H(k) = \sum_{m=0}^{M-1} c_m \left(2 - \delta_{m0}\right) \sum_{n=0}^{(N-1)/2} \left(2 - \delta_{n0}\right) \cos\left(\frac{2\pi mn}{N}\right) \cos(kn) = \sum_{m=0}^{M-1} c_m B_m(k), \tag{14}$$

where

$$B_m(k) = \left(2 - \delta_{m0}\right) \sum_{n=0}^{(N-1)/2} \left(2 - \delta_{n0}\right) \cos\left(\frac{2\pi mn}{N}\right) \cos(kn) \tag{15}$$

are the Fourier transformed basis functions. By matching the l^{th} even derivative at $k = 0$, we obtain the linear equation:

$$\sum_{m=0}^{M-1} c_m B_m^{(2l)}(0) = D^{(2l)}(0), \tag{16}$$

which is a system of linear equations that can be solved to determine c_m. Then c_m is used in Equation 14 to obtain $H(k)$, which can be transformed to h_n by applying inverse Fourier transforms.

Stabilizing the Hale's extrapolator

To implement and investigate Hale's method, a subroutine was written to design an extrapolation filter for a given filter length, frequency, and velocity. As a calibration test for the subroutine, some of the key figures in Hale's paper were reproduced with the same parameters. Figure 2 shows the amplitude spectrum of

- the desired transform, $|D(k)|$ (blue),
- the extrapolation filter based on the conventional Taylor series approach (red),
- and the extrapolation filter, $|H(k)|$, based on Hale's approach (green).

Figure 2 shows that the conventional Taylor series filter will have amplitudes greater than one for the evanescent wavenumbers. Applying this filter recursively will cause all

amplitudes greater than one to grow exponentially as the wavefield is extrapolated into the subsurface. On the other hand, Hale's extrapolation filter is stable for all evanescent wavenumbers. This means that these amplitudes will exponentially decay when applying the extrapolation filter recursively.

In order to implement Hale's extrapolator, we have to specify M terms to match the terms in the truncated Taylor's series of the desired transform such that

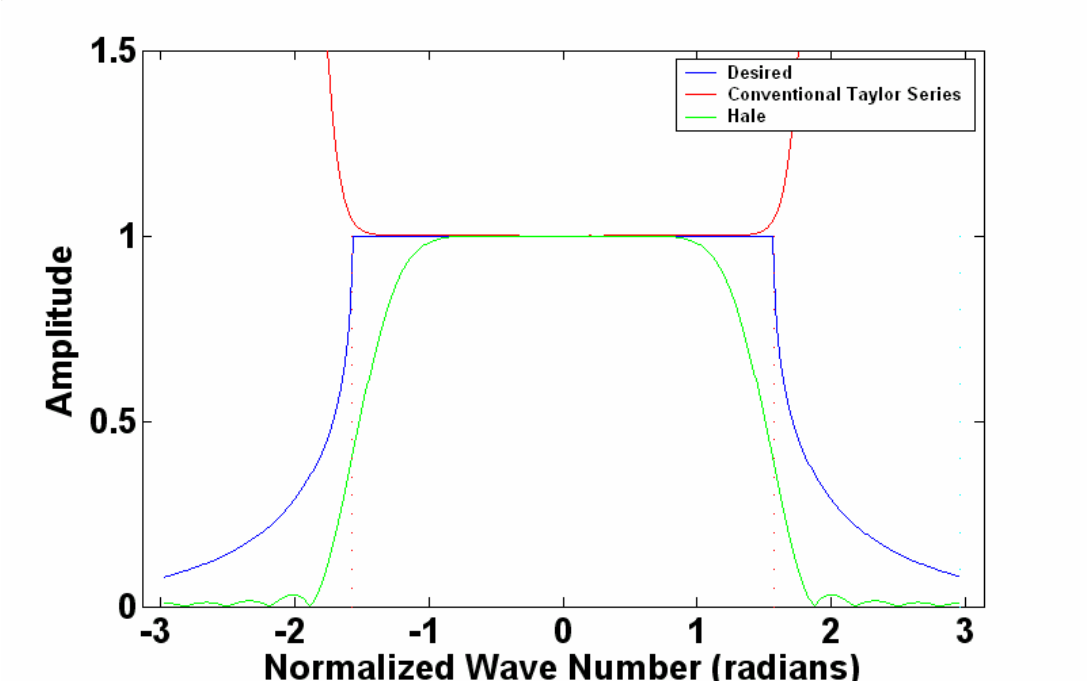

FIG 2. Amplitude spectra of the exact, truncated Taylor series, and Hale operators. This was calculated for the normalized frequency: $\omega\Delta x/v = \pi/2$ and $\Delta x = \Delta z$ =10 m. Note that wavenumbers greater than $\pi/2$ (see the dashed line) correspond to evanescent waves.

$$M \le N \tag{17}$$

and

$$\left|H(\mathrm{k})\right| \le 1. \tag{18}$$

There is no direct formula for choosing the optimum M to ensure stability. Further, choosing a constant M value will cause some normalized frequencies to be unstable (Figure 3).

To make this filter stable for all normalized frequencies, different normalized frequencies should have different M values. By breaking the normalized frequencies into small ranges and assigning a different M for each range, stability was ensured for all normalized frequencies. These higher normalized frequencies will be assigned larger M values than the low ones. Figure 4 shows that when varying the M value with the normalized frequencies, the filter exhibits stability for all normalized frequencies.

Figure 5 shows a comparison between the amplitude and phase spectra of the desired transform with Hale's filter. Note that the amplitude of the desired transform has a sharp drop at the evanescent boundary. On the other hand, this boundary is tapered in Hale's filter. Furthermore, there is a sharp decrease in amplitude when the normalized wavenumber is just greater than the normalized frequency. Also, the decrease in amplitude occurs smoothly and starts before the evanescent boundary in Hale's filter.

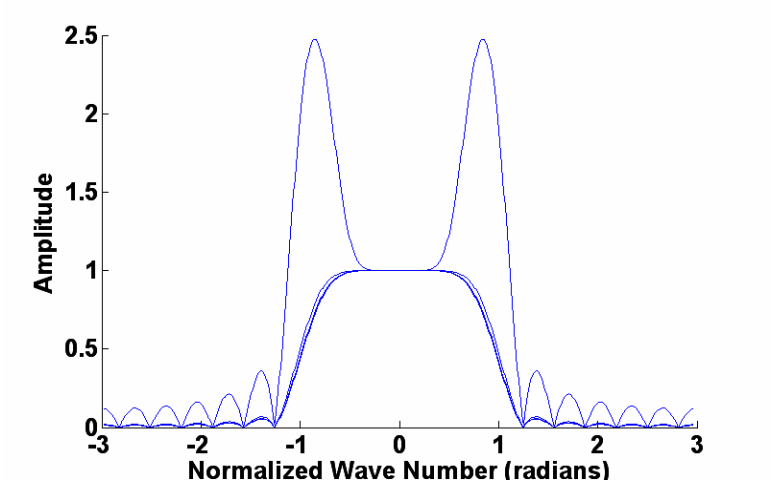

FIG 3. Amplitude spectra of the Fourier transforms of Hale's filters for different normalized frequencies with constant M. Note that it is unstable for some normalized frequencies. The frequencies are from 10-100 Hz incrementing by 10 Hz, v=2000 m/s, dx=dz=10 m, and M=5.

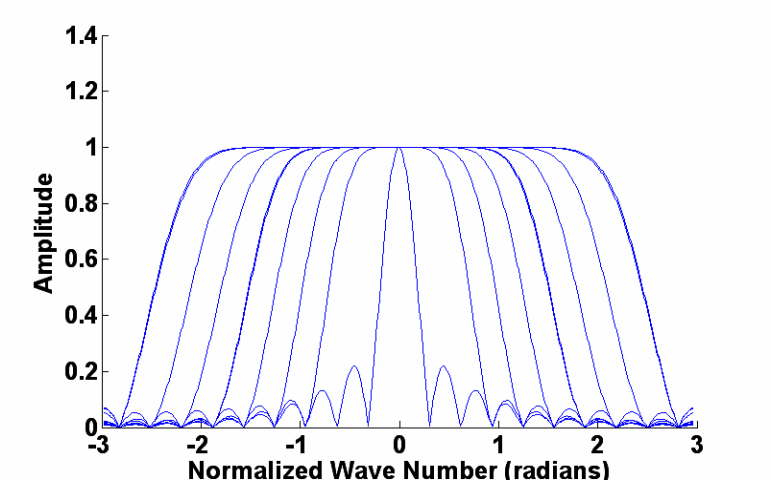

FIG 4. Amplitude spectra of the Fourier transform of Hale's filters for different normalized frequencies after varying *M* with the normalized frequencies. The frequencies are from 10-100 Hz incrementing by 10 Hz, v=2000 m/s, $\Delta x = \Delta z = 10m$, and *M*=1-8 depending on the value of $2 * pi * f * \Delta x / v$. For small values of $2 * pi * f * \Delta x / v$, *M* tends to be small and large for big values of $2 * pi * f * \Delta x / v$.

In Figure 5, the phases of the desired transform and Hale's filter are quite similar in the non-evanescent region. In fact, the similarity increases as we move away from the boundary and decreases as we near the boundary. In the evanescent region, they are

totally different. Furthermore, this discrepancy occurs before the start of evanescent region.

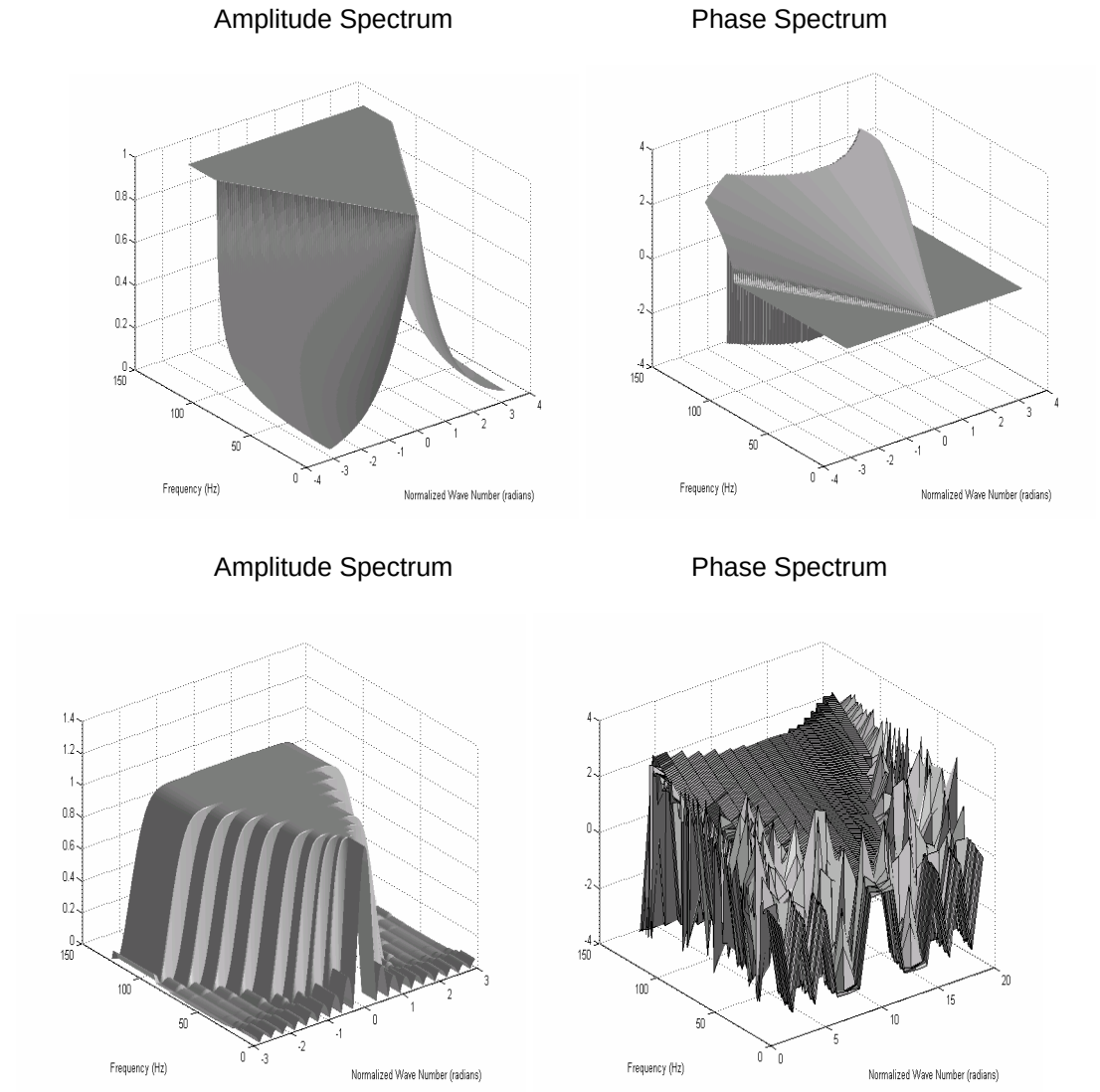

FIG 5. Phase and amplitude spectra of the Fourier transforms of the desired transform (top) and Hale's extrapolation operators. This is for a constant velocity medium of 2000 m/s, $\Delta x = \Delta z = 10$, and a sample rate of 4 ms.

Impulse response of Hale's extrapolator

Figure 6 shows four non-zero points in the time domain. Using Hale's extrapolation operator with 19-coefficients, the four points in the time domain were migrated into four semicircles in the depth domain (Figure 7). However, note that the steep dips were

attenuated due to a low number of coefficients. A longer operator is needed to migrate steeper dips. This impulse response test shows that the Hale's extrapolator is fairly stable at least for this depth range.

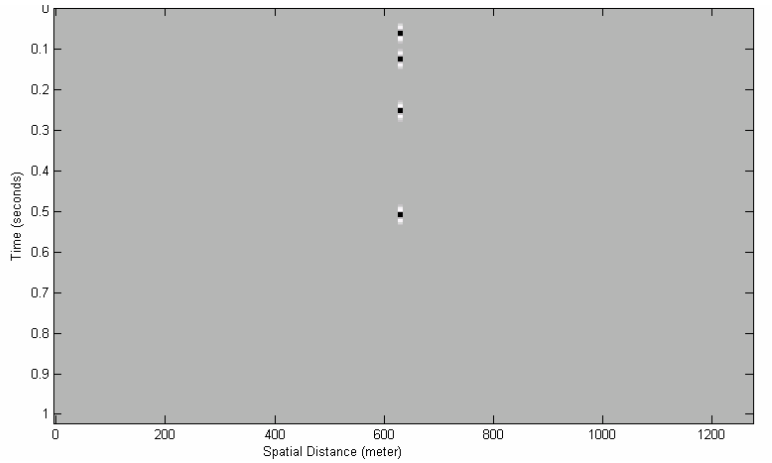

FIG 6. Three non-zero points in the time domain. This is for a constant velocity medium of 2000 m/s, $\Delta x = \Delta z = 10$, and a sample rate of 4 ms.

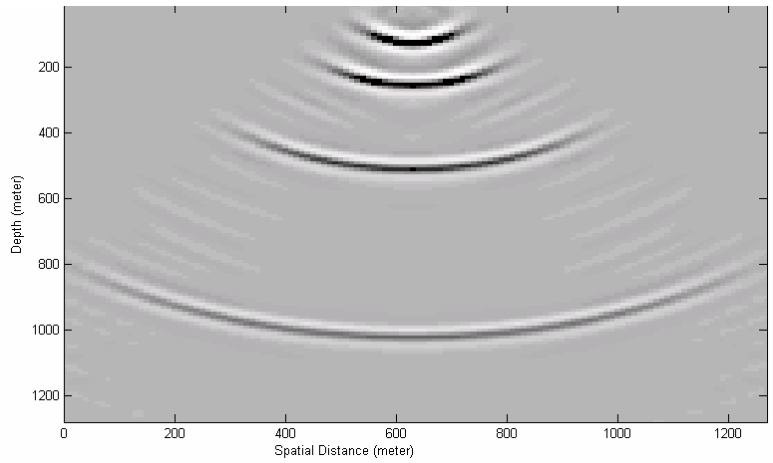

FIG 7. Impulse responses after migration using Hale's extrapolation filter with 19-coefficients.

Poststack migration of Marmousi data using Hale's extrapolator

To investigate the behavior of Hale's extrapolator in the presence of lateral velocity variations, the Marmousi dataset is used. The Marmousi data have strong lateral velocity variations and steeply dipping events. Despite the fact that poststack migration is not enough to place events in their correct lateral position, a poststack migration test shows how Hale's extrapolator behaves in the presence of lateral velocity variations and steep

dipping events. Figure 8.a shows the velocity model and Figure 8.b shows the unmigrated time section. Figure 8.c shows the migration result using Hale's extrapolator. Whilst Hale's extrapolator could handle the lateral velocity variation, the steeply dipping events were not properly migrated. Also, the image shows that the extrapolator is fairly stable.

(a)

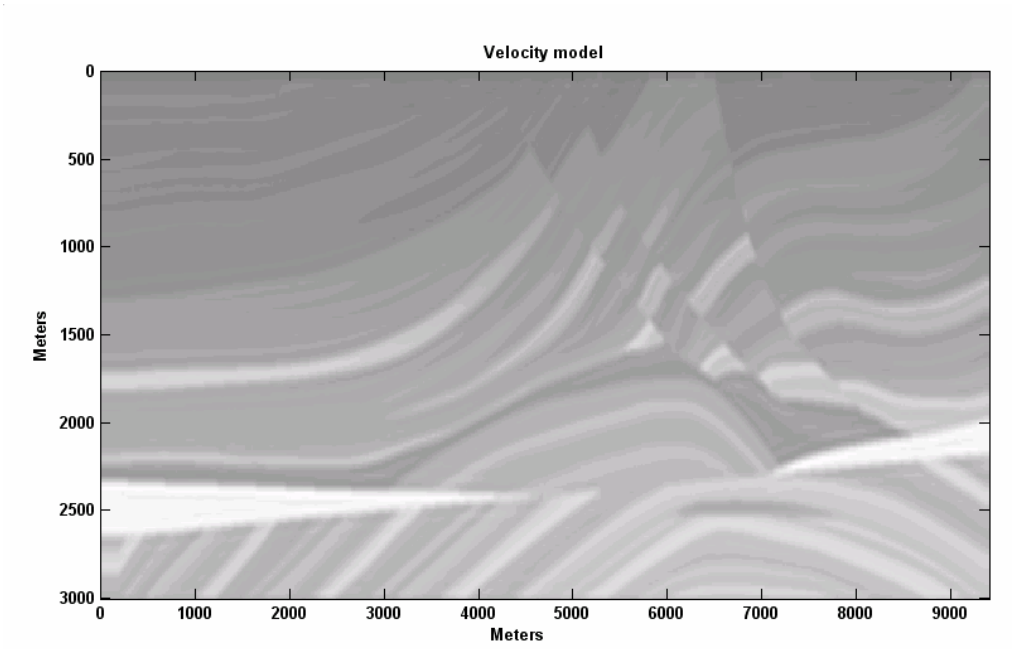

(b)

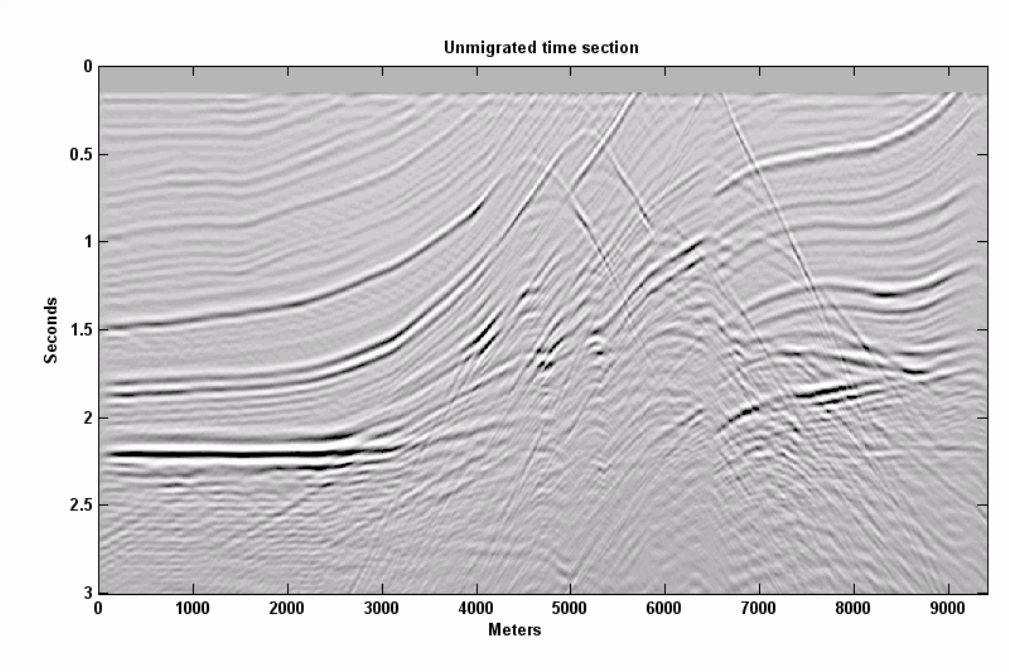

(c)

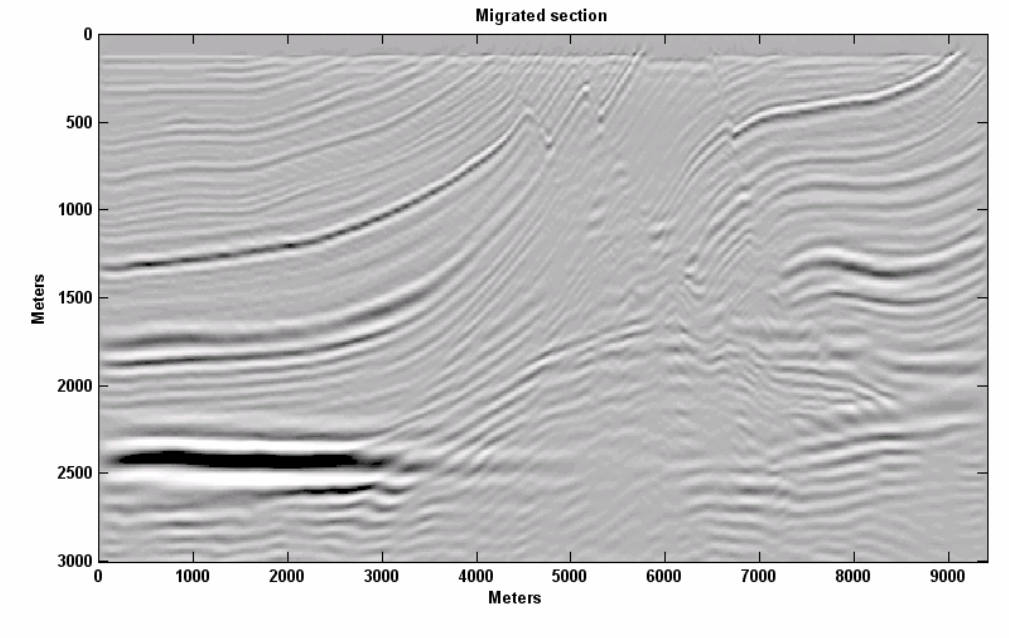

FIG 8. (a) The velocity model, (b) the unmigrated time section, and (c) the migrated section using Hale's extrapolator with 19 coefficients.

INVESTIGATING DIFFERENT PRESTACK MIGRATION METHODS

A brief review of different constant velocity prestack depth migration approaches is presented here. The different investigated methods are:

- prestack Kirchhoff depth migration,
- prestack depth migration with Claerbout's imaging conditions, which are:
  - deconvolution imaging condition,
  - and cross-correlation imaging condition,
- and prestack depth migration with time excitation imaging condition.

Prestack Kirchhoff Depth Migration

To perform a constant velocity prestack Kirchhoff migration, the following equation can be used

$$\underset{(2-D)}{\hat{R}_{\theta}}\left(x_G, x_s\right) = \frac{2}{c_0}\int_{x_G} dx \left\{\frac{\sqrt{2\pi\sigma_{Gs}}}{\sqrt{2\pi\sigma_{gG}}}\cos\theta_{gG}\right\} 2\,\mathrm{Re}\left[\underset{(2-D)}{\frac{1}{2\pi}\int_0^{\infty} d\omega S(\omega)(\omega)\, P_S}\left(x_g, x_s, \omega\right) e^{-i\omega\left(r_{Gs}+r_{gG}\right)/c_0}\right], \tag{19}$$

where

x_g = receiver location,

x_s = source location,

ω = angular frequency,

$\hat{R}_{\theta}\left(x_{G,} x_s\right)$ = angle dependant reflectivity,

$\mathrm{x_G}$ = x-location of the image point in the subsurface,

$\mathrm{z_G}$ = depth of the image point in the subsurface,

$r_{\mathrm{gG}} = \sqrt{\left(\mathrm{x_g} - x_G\right)^2 + \left(z_g - z_G\right)^2}$,

$r_{\mathrm{Gs}} = \sqrt{\left(\mathrm{x_s} - x_G\right)^2 + \left(z_s - z_G\right)^2}$,

c_0 = velocity,

$\sigma_{Gs} = c_0 r_{Gs}$,

$\sigma_{gG} = c_0 r_{gG}$,

θ_{gG} = acute angle between the ray direction from the receiver and surface normal,

$S(\omega)$ = source spectrum,

and $P_S\left(x_g, x_s, \omega\right)$ = recorded wavefield at the geophones.

Figure 9 shows a symmetric split spread shot gather. A shot was fired above a horizontal reflector at depth 500 m. The receiver spacing is 10 m and the sample rate of 4 ms.

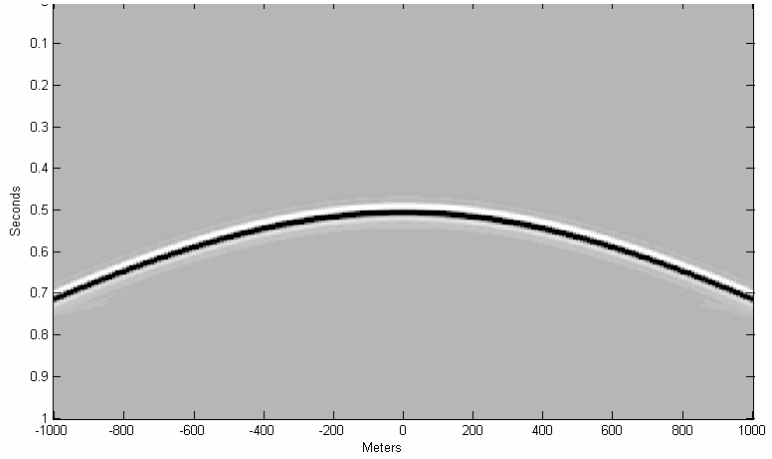

FIG 9. A Shot gather with a flat horizontal reflector where v=2000 m/s and the depth of the reflector is 500 m.

Figure 10 shows the image after using prestack Kirchhoff depth migration. The reflection was imaged at the correct depth. But the image is contaminated with artifacts.

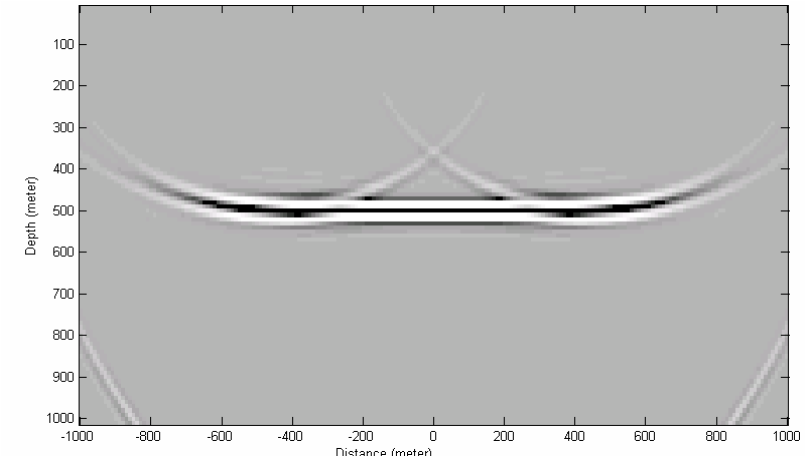

FIG 10. After prestack Kirchhoff depth migration. Reflector was imaged to the correct depth at 500 m but the image is contaminated with migration artifacts.

The artifacts that are seen on the image in Figure 10 are due to the truncation of the summation hyperbolas. In order to avoid the creation of any artifacts during migration, the sides of the summation hyperbolas must traverse the band limited data (Figure 11). If the flank of the summation hyperbola completely crosses the band limited data zone, a proper cancellation of amplitudes will occur. On the contrary, if any flank of the summation hyperbola truncates inside the band limited data zone, some amplitude will be picked up and mapped to the wrong depth creating an artifact (Figure 11).

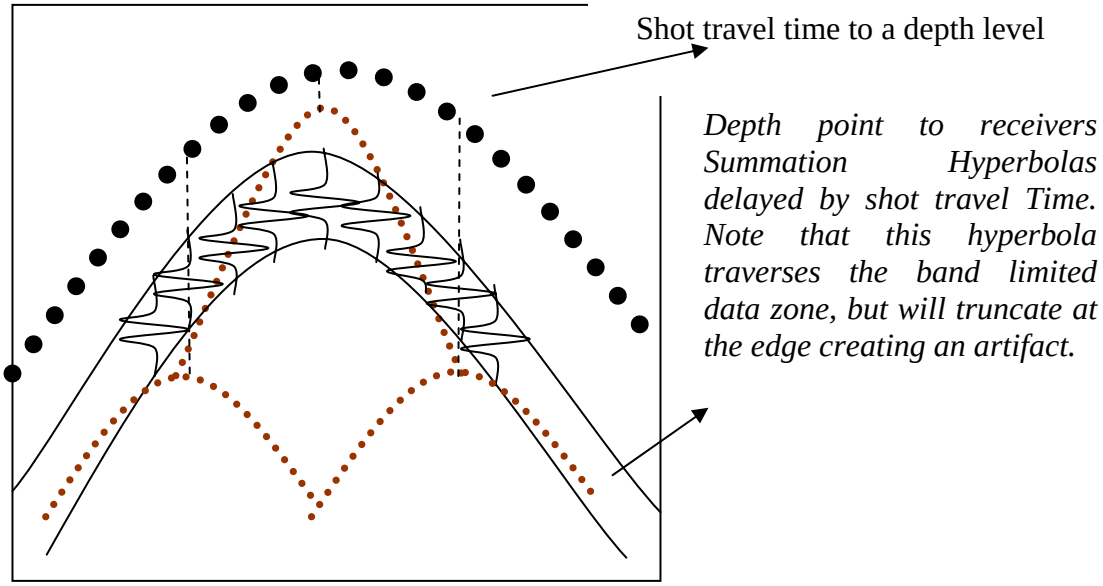

FIG 11. To avoid artifacts, the summation hyperbolas must completely traverse the band limited data (2*T*). If the summation hyperbolas truncate inside the band limited data, an artifact will be created.

One way to minimize the effects of artifacts is to apply a taper prior to summation. From this equation

$$\underset{(2-D)}{\hat{R}_{\theta}}\left(x_G, x_s\right) = \frac{2}{c_0}\int_{x_G} dx \left\{\frac{\sqrt{2\pi\sigma_{Gs}}}{\sqrt{2\pi\sigma_{gG}}}\cos\theta_{gG}\right\} 2\,\mathrm{Re}\left[\underset{(2-D)}{\frac{1}{2\pi}\int_0^{\infty} d\omega S(\omega)(\omega)\, P_S}\left(x_g, x_s, \omega\right) e^{-i\omega\left(r_{Gs}+r_{gG}\right)/c_0}\right], \tag{20}$$

the summation is over dx to create one trace on the image space. Applying a taper prior to the summation can weaken the artifacts. Figure 12 shows a comparison between un-tapered and tapered image gathers. These image gathers are different than the image gathers obtained from migrating different shots and known in literature as CIG (common image gather).

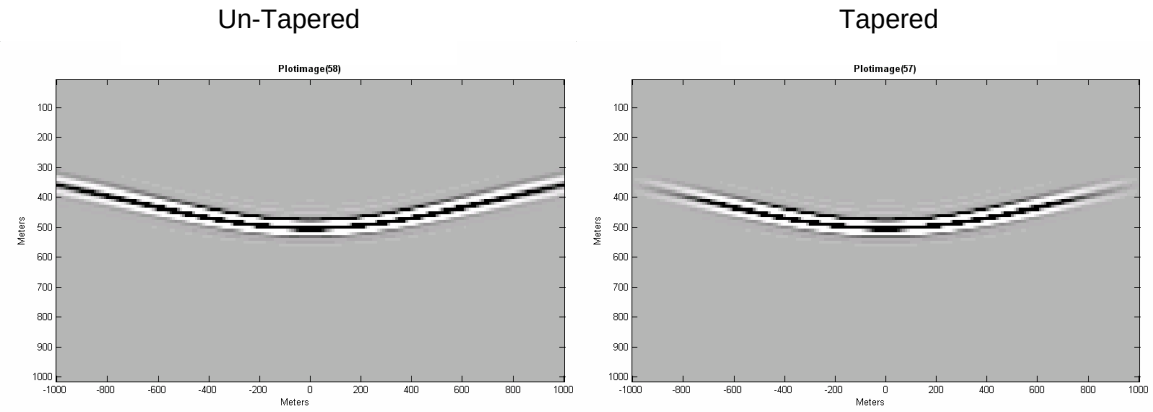

FIG 12. Image gathers without a taper (on the left) and with a taper on the right.

Figure 13 shows the result after applying a taper prior to summing the image gathers. The taper was very effective in minimizing the effect of the artifacts. The image obtained from the tapered gathers has fewer artifacts. This is one way to eliminate migration artifacts.

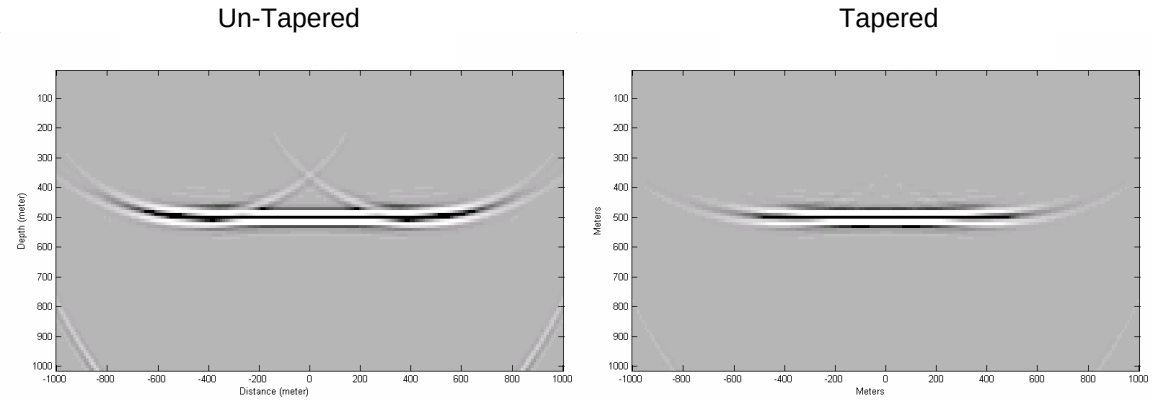

FIG 13. Applying a taper to the image gathers has minimized the effects of the artifacts and improved the image.

Prestack depth migration with Claerbout's imaging condition

In this section, a brief review of the prestack depth migration approach using the reflector mapping concept is presented. This review will give some insight about these methods and which ones preserve reflector amplitudes. The principle of reflector mapping was first introduced by Claerbout in 1971. The basic principle of reflector mapping is that reflectors exist in the subsurface when the first arrival of the downgoing wave is time coincident with the upgoing wave. This can give the correct phase but not the amplitude at the reflector. To get the correct amplitude at the reflector, Claerbout defines it as the ratio of the upgoing and downgoing wavefields at the subsurface imaging location.

Geiger (2001) derived Claerbout's reflector mapping as a reformulation of the Kirchhoff integral. Under ideal conditions (no noise), Geiger (2001) derived

$$\hat{R}_\theta\left(x_G, x_s\right) = \frac{1}{2\pi}\int_{-\infty}^{\infty} d\omega \frac{P_S^{-}\left(x_G, x_s, \omega\right)}{P_i^{+}\left(x_G, x_s, \omega\right)} d\omega, \tag{21}$$

which can estimate a true reflectivity map based on Claerbout's imaging condition and the deconvolution imaging condition is defined where $P_S^{-}\left(x_G, x_s, \omega\right)$ is the upward extrapolated wavefield that was recorded at the surface for a subsurface location, x_G and $P_i^{+}\left(x_G, x_s, \omega\right)$ is the downward modeled source from the surface to x_G.

To avoid dividing by zero, Claerbout suggested multiplying Equation 21 by the conjugate of the incident wavefield such that

$$\hat{R}_\theta\left(x_G, x_s\right) = \frac{1}{2\pi}\int_{-\infty}^{\infty} d\omega \frac{P_S^{-}\left(x_G, x_s, \omega\right)}{P_i^{+}\left(x_G, x_s, \omega\right)} \frac{\left(P^{+}\left(x_G, x_s, \omega\right)\right)^{*}}{\left(P^{+}\left(x_G, x_s, \omega\right)\right)^{*}}. \tag{22}$$

Now, the denominator is real and does not affect the phase it can be eliminated, leading to the cross-correlation imaging condition

$$\hat{R}_\theta\left(x_G, x_s\right) = \frac{1}{2\pi}\int_{-\infty}^{\infty} d\omega P_S^{-}\left(x_G, x_s, \omega\right)\left(P_i^{+}\left(x_G, x_s, \omega\right)\right)^{*}, \tag{23}$$

where $P_S^{-}\left(x_G, x_s, \omega\right)$ is the extrapolated wavefield that was recorded at the surface for a subsurface location, x_G and $P_i^{+}\left(x_G, x_s, \omega\right)$ is the modeled source from the surface to x_G. This should give the correct phase but not the amplitude, as we shall see. For this project, a monopole 2-D Green function will be used as the incident wavefield

$$P_i^{+}\left(x_G, x_s, \omega\right) = \underset{(2-D)}{\vec{G}}\left(x_G, x_s, \omega\right), \tag{24}$$

where

$$\underset{(2-D)}{\vec{G}}\left(x_G, x_s, \omega\right) \approx \frac{\sqrt{2\pi\sigma}}{\sqrt{-i\omega}} \frac{e^{i\omega r / c_0}}{4\pi r}, \tag{25}$$

note that the incident wavefield has a geometrical spreading term, phase rotation, and frequency filter.

Prestack depth migration with time excitation imaging condition

Inserting Equation 25 into Equation 23 and omitting the amplitude, phase rotation, and frequency filter terms results in the shot excitation method

$$\hat{R}_\theta\left(x_G, x_s\right) = \frac{1}{2\pi}\int_{-\infty}^{\infty} d\omega P_S^{-}\left(x_G, x_s, \omega\right) e^{-i\omega r/c_0}, \tag{26}$$

this corresponds to a delayed delta function in the time domain. This will give the correct phase of the reflector but not the amplitude.

Which method is a true amplitude prestack depth migration?

These three imaging conditions will give the correct phase but each will treat the amplitude in a different way. The next example illustrates that point.

Let's assume that we have four reflectors in the subsurface at 200 m, 400 m, 800 m, and 1600 m. Assume we fire a shot over that model and the rays are normally incident to the reflectors (Figure 14). Let's also assume that we are dealing with 3-D data and we have the 3-D Green function as the incident wavefield

$$\underset{(3-D)}{\vec{G}}^{+}\left(x_G, x_s, \omega\right) = \frac{e^{i\omega r/c_0}}{4\pi r} \tag{27}$$

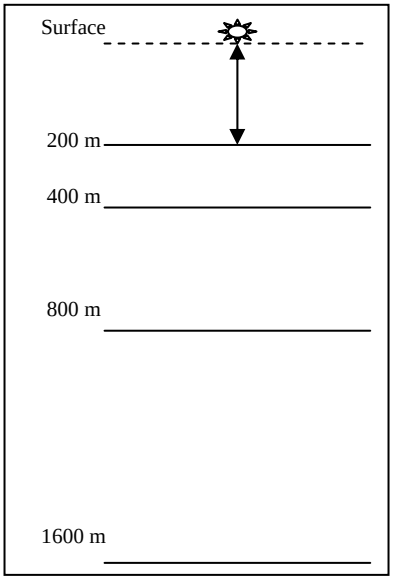

FIG 14. A shot was fired over four reflectors. We will assume that the rays are normally incident to each reflector. Table 1 will show the amplitude changes at each reflector.

Table 1. Summary of the amplitude changes at each reflector and the difference among the three imaging conditions: deconvolution, cross-correlation, and time excitation imaging conditions. This table assumes that there is no transmission loss and the *R* is the same for each reflector.

	U	U^-	D^+	D^{++}	U^-/D^+	$U^- * \left(D^+\right)^*$	$U^- * \left(D^{++}\right)^*$
200 m	RA	$2RA$	$2A$	1	R	$4RA^2$	$2RA$
400 m	$R\frac{A}{2}$	RA	A	1	R	RA^2	RA
800 m	$R\frac{A}{4}$	$R\frac{A}{2}$	$\frac{A}{2}$	1	R	$\frac{RA^2}{4}$	$R\frac{A}{2}$
1600 m	$R\frac{A}{8}$	$R\frac{A}{4}$	$\frac{A}{4}$	1	R	$\frac{RA^2}{16}$	$R\frac{A}{4}$

$A = \frac{1}{(4\pi(400))}$,

R=reflection coefficient,

U = recorded wavefield at the geophones,

U^- = extrapolated wavefield to the reflector,

D^+ = incident wavefield at the reflector by using a 2-D Green function,

D^{++} = incident wavefield at the reflector by using a delta function (excitation time imaging condition),

U^-/D^+ = deconvolution imaging condition,

$U^- * \left(D^+\right)^*$ = cross-correlation imaging condition,

$U^- * \left(D^{++}\right)^*$ = excitation time imaging condition.

- From Table 1, we can see that only the deconvolution imaging condition will be able to give the correct amplitude of the reflector at each interface. On the other hand, the others will give the correct phase but not the amplitude. Thus, the deconvolution imaging condition is a true amplitude prestack depth migration. Figure 15 shows true amplitude shot gather with seven horizontal reflectors. Note how their amplitudes weaken with depth.

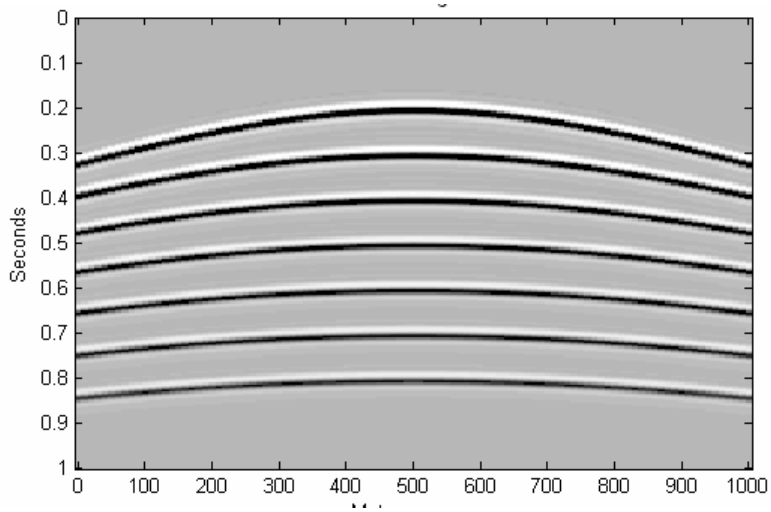

FIG 15. A shot gather with true amplitudes. Note how reflections weaken with depth.

This model will be migrated with

- prestack Kirchhoff depth migration,
- prestack depth migration with Claerbout's imaging conditions:
    - deconvolution imaging condition,
    - cross-correlation imaging condition,
- prestack depth migration with the time excitation imaging condition.

Figure 16 shows the migration result. Only the prestack Kirchhoff and the depth migration with the deconvolution imaging condition were able to give the correct amplitude for each reflector.

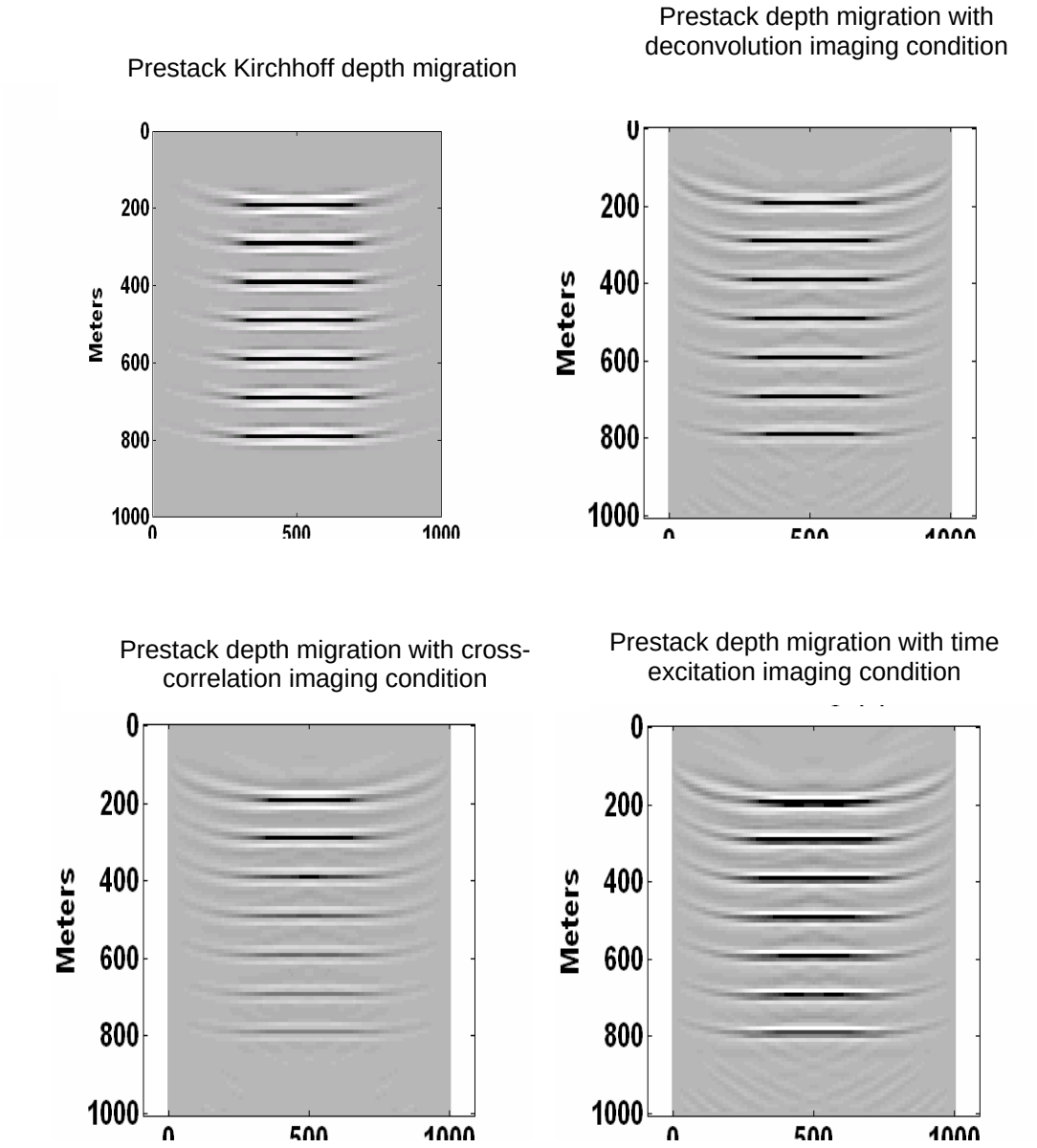

FIG 16. Migration of the shot gather in Figure 15 with Kirchhoff migration and the three imaging conditions.

CONCLUSIONS

In this report, a brief review of Hale's extrapolator was shown. Hale's extrapolator is not stable when the number of terms matching the terms in the truncated Taylor's series of the desired transform, *M*, is kept fixed for all normalized frequencies. The only way to stabilize the extrapolator is to vary *M* with the value of the normalized frequency. Higher normalized frequencies should be assigned higher *M* values than the lower ones. The difficulty with that is that there is not a direct formula to do compute *M*, and assigning *M* values is based on trial and error. This is one of the disadvantages of this extrapolator.

On the other hand, the poststack migration of the Marmousi dataset using Hale's extrapolator shows that it can handle lateral velocity variations but not the steeply dipping events.

Also in this report, different migration methods using Hale's extrapolator were investigated, and not all of them could preserve the reflector's amplitude. Only the prestack Kirchhoff depth migration and prestack depth migration using Hale's extrapolator with the deconvolution imaging condition were true amplitude methods.

ACKNOWLEDGEMENTS

We wish to thank the sponsors of the CREWES project.

REFERENCES

Claerbout J.F., 1971, Toward a unified theory of reflector mapping: Geophysics: **36**, 467-481.

Gazdag, J., 1978, Wave equation migration with the phase shift method: Geophysics: **43**, 1342 – 1351.

Geiger, H. D., 2001, Relative-Amplitude-Preserving Prestack Time Migration by the Equivalent Offset method: PhD Thesis.

Hale, D., 1991, Stable Explicit Depth Extrapolation of Seismic Wavefield. Geophysics: **56**, 1770-1777.

Holberg, O., 1988, Twoardes optimum one-way wave propagation: Geophys. Prosp.: **36**, 99-114. Expl. Geophys., Expanded Abstracts, 1599-1602.

Thorbecke, J. W., Wapenaar, K., Swinners, G., 2004, Design of one-way wavefield extrapolation operators, using smooth functions in WLSQ optimization: Geophysics: **69**, 1037-1045.